Energy Sinks for Lee Waves in the Northern South China Sea

Zhinbin Yang[1], Zhao Jing[1,2], and Xiaoming Zhai[3]

[1]Frontier Science Center for Deep Ocean Multispheres and Earth System (FDOMES) and Physical Oceanography Laboratory, Ocean University of China, Qingdao, China.

[2]Qingdao National Laboratory for Marine Science and Technology, Qingdao, China.

[3]Centre for Ocean and Atmospheric Sciences, School of Environmental Sciences, University of East Anglia, Norwich, United Kingdom.

Corresponding author: Zhao Jing (jingzhao198763@sina.com)

Xiaoming Zhai (xiaoming.zhai@uea.ac.uk)

Key Points:

- The sink of lee waves in the northern SCS is investigated in a high-resolution nested model with a synthetically-generated rough topography
- The wave dissipation is the dominant sink of lee wave energy, with wave energy re-absorption by mean flows being of secondary importance
- The dominant direction of energy transfer is from mean flows to lee waves through vertical shear and horizontal strain of mean flows

Abstract

Recent observations report a discrepancy between observed energy dissipation rates and lee wave pressure flux predicted by linear theory in the Southern Ocean, raising the possibility that wave energy re-absorption by mean flows may be an important route to wave energy sink. Here we investigate the sink of lee waves in the northern South China Sea in a high-resolution nested model initialized with a synthetically-generated rough topography. Our results indicate that wave dissipation is the dominant sink of lee wave energy, with wave energy re-absorption being of secondary importance. The dominant direction of energy transfer is from mean flows to lee waves through vertical shear and horizontal strain of mean flows. A series of idealized experiments suggest that the weak wave energy re-absorption in the northern South China Sea is primarily due to the large Froude number there.

Plain Language Summary

The interaction of ocean flows with small-scale topographic obstacles can generate internal waves known as lee waves which then propagate away from the topography into the ocean interior and lead to turbulence and enhanced mixing when they break. However, recent studies argue that a large fraction of the wave energy is returned to the mean flows via wave-mean flow interaction. Here we investigate the sink of lee waves in the northern South China Sea both in a high-resolution nested model and a series of idealized model experiments. Our model results show that the dominant sink of lee wave energy in the northern South China Sea is wave dissipation, with wave energy re-absorption by the mean flows being of secondary importance.

1 Introduction

The generation of oceanic lee waves over small-scale topographic obstacles can extract energy from the geostrophic flow, and result in enhanced turbulent energy dissipation and mixing. They are thought to be an efficient route for ocean energy dissipation and deep ocean mixing (Marshall & Naveira Garabato, 2008; Naveira Garabato et al., 2004; Nikurashin et al., 2013; Yang et al., 2021). Global estimates of energy conversion rate from geostrophic flows into lee waves in the ocean range from 0.2 to 0.75 TW, accounting for an important portion of the ocean energy cycle (Nikurashin & Ferrari, 2011; Scott et al., 2011; Wright et al., 2014).

Recent observations in the Southern Ocean (e.g., Brearley et al., 2013; Sheen et al., 2013; Waterman et al., 2013) suggest that the observed levels of energy dissipation in the bottom 1 km can be smaller by up to an order of magnitude than that implied by lee wave pressure flux predicted by the linear theory. Several potential explanations for this discrepancy have been discussed by Kunze and Lien (2019), including sampling biases (Klymak, 2018), poorly observed bottom flow or topography characteristics (Trossman et al., 2015), wave energy re-absorption by mean flows (R_{IW}) via wave-mean flow interaction (Waterman et al., 2014) and non-local dissipation of lee waves due to mean flow advection (Zheng & Nikurashin, 2019). In addition, tides have also been shown to have a suppression effect on the lee wave pressure flux (Shakespeare, 2020). Importantly, different explanations/mechanisms imply different energy dissipation rates and levels of mixing. For example, if the energy of lee waves is mostly re-absorbed by mean flows, they would not represent an energy sink of mean flows nor a source of deep ocean mixing; downstream advection by mean flows regulates the geographical distribution of energy dissipation rate associated with lee waves but does not necessarily change its overall magnitude.

The R_{IW} may be particularly relevant in regions characterized by bottom-enhanced mean flow velocities (e.g., the Southern Ocean). However, in most regions of the ocean, the mean flow vertical structure is characterized by flow speed decreasing towards the sea floor, in which case the energy transfer is directed from mean flows to lee waves (Baker & Mashayek, 2021; Sun et al., 2022). Using a realistic global ocean model with lee wave drag closure, Eden et al. (2021) estimated the global energy transfer between lee waves and mean flows and suggested that the dominant energy transfer is from mean flows to lee waves, although their estimates depend on parameter choices for the nonlinear effects. If the finding of Eden et al. (2021) is true for the global ocean, it indicates that the role of lee waves in ocean energy dissipation and mixing may have been underestimated, since wave-mean flow energy exchanges have not yet been considered in the existing estimates of lee wave energy conversion rates (e.g., Nikurashin & Ferrari, 2011; Scott et al., 2011; Wright et al., 2014). In addition, the R_{IW} may be potentially dependent on the Froude number $Fr = Nh/U_b$ where h is the root-mean-squared height of the topography and U_b is the bottom flow speed. Inertial oscillations (IOs) can be triggered by wave breaking in a rotating frame and the rapid growth of IOs under large Fr condition could significantly modify the wave vertical scales and promote wave breaking (Nikurashin & Ferrari, 2010a; Zemskova & Grisouard, 2021). This indicates that lee waves generated in a large Fr environment tend to dissipate close to the rough topography and consequently they are less likely to interact with mean flows and be re-absorbed by mean flows.

Here we investigate the energy sinks of lee waves in the northern South China Sea (SCS) using a combination of a high-resolution ($\triangle x$ ~500 m) realistic model and a series of idealized model experiments. The northern SCS is characterized by layered and surface-intensified currents, typical of flow structures in many regions of the world ocean and the Fr there is generally larger than one due to the weak bottom mean flow. The remainder of this paper is organized as follows. We begin in section 2 by describing the model setup and experimental design. In section 3, we calculate the lee wave energy budget and investigate the potential mechanisms for wave-mean flow interaction. Sensitivities of our results to the Froude number and the flow structure are discussed in section 4. Finally, the paper concludes with a summary in section 5.

2 Methodology

2.1 Model configurations

A Massachusetts Institute of Technology general circulation model (MITgcm; Marshall et al., 1997) is adopted to simulate the mesoscale eddies and their dissipation in the northern SCS (Yang et al., 2022). The model is a three-level nested system with a parent grid resolution of $\triangle x$ = 1/24° (hereinafter P1) covering most of the Northwest Pacific Ocean and successive child grids with $\triangle x$ = 1/72° for the SCS (hereinafter C1) and $\triangle x$ = 1/216° for the northern SCS (hereinafter C2, Figure 1). In order to resolve the small-scale wave motions, C1 and C2 also have a vertical resolution refinement with maximum $\triangle z$ = 30 m. For all the three nested models, the harmonic Leith and modified bi-harmonic Leith coefficients are set to be 1.2 and 1.5. The bi-harmonic temperature/salinity diffusion coefficient is chosen to be 1×10^8 m^4/s at 1/24° resolution and reduced by a factor of ten for each tripling in resolution. No harmonic horizontal diffusivity is used. We employ the K-profile parameterization (KPP) vertical mixing scheme (Large et al., 1994) and a quadratic bottom friction with a drag coefficient of Cd = 0.0021. P1 and C1 are driven by daily atmospheric forcing constructed from climatology outputs of ERA-Interim (Dee et al., 2011). The atmospheric forcing for C2 is the same as P1 and C1, except that the monthly-varying ERA-Interim wind forcing is used in order to eliminate the generation of wind-induced near-inertial waves. There is no tidal forcing applied at the model lateral boundaries.

In C2 simulation, synthetically generated small-scale (< 20 km) rough topography based on the observed topographic spectrum of the SCS (Goff & Jordan, 1988) is added to the low-pass filtered (> 20 km) realistic topography, but only in regions deeper than 500 m to avoid the outcrop of the super-imposed topography. The low-pass filtered topography is constructed from the SRTM30_PLUS dataset with a grid size of 1/120° (Becker et al, 2009). To avoid the lateral boundary effects, a region 2° away from the nest boundary of C2 simulation is chosen for analysis in this study (dashed white line in Figure 1). The modelled surface eddy field and the near-bottom current velocities generally compare well with the observations and data-assimilated models. Detailed model configurations can be found in Yang et al. (2022).

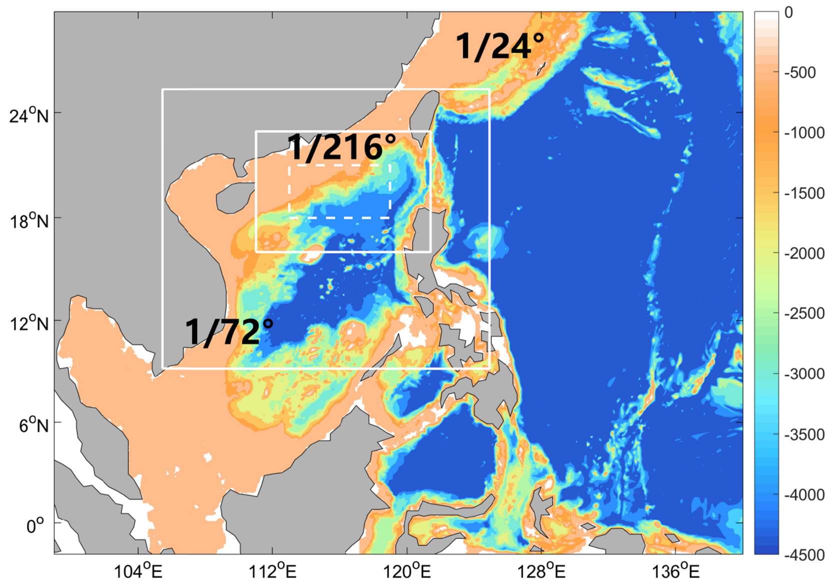

Figure 1. Bathymetry (m) used in P1 simulation ($\triangle x$ = 1/24°). The boundaries of the successive nested model domains of C1 ($\triangle x$ = 1/72°) and C2 ($\triangle x$ = 1/216°) are delineated by white solid lines. The dashed white line inside C2 indicates the region selected for analysis (Section 3).

2.2 Decomposition of ocean current into wave and mean flow components

The intrinsic phase velocity of lee waves is equal in magnitude but opposite in direction to the mean flow velocity so that they are stationary in an Eulerian frame owing to Doppler shifting. For this reason, we decompose the velocity and buoyancy fields ($\mathbf{u}$ and b) into the wave and mean flow components in a Lagrangian frame (Nagai et al., 2015; Shakespeare & Hogg, 2017; Yang et al., 2021; Yang et al., 2022).

Over 70 million flow-following floats (one float per model cell, but five floats in the bottom-most 5 levels) are introduced in the C2 experiment and their trajectories are saved hourly over the 6-day analysis period (May 18th-23rd). This 6-day period is chosen because the volume-integrated energy dissipation during these 6 days is close to its annual average. The paths of these floats are computed online. Note that only the horizontal velocities are used for float advection (i.e., semi-Lagrangian). We first apply a high-pass filter (higher than the local inertial frequency f) to $\mathbf{u}$ and b following each float trajectory and then interpolate the filtered quantities back onto the model grid every half day. The wave ($\mathbf{u}'$ and b') and mean flow field ($\overline{\mathbf{u}}$, $\overline{b}$) are defined as the interpolated high-frequency and low-frequency components, respectively. To avoid the ringing effect, only the middle 4 days of the filtered data are used. A detailed description of the Lagrangian filter method can be found in Yang et al. (2022).

The Lagrangian filtering provides a reliable way to separate the wave and mean flow motions in our simulations. To demonstrate this, we compare the horizontally-averaged vertical kinetic energy spectra in the Lagrangian and Eulerian frames above the 3000-m isobath (Figure 2). The Lagrangian spectrum is computed as the average spectra of the floats whose initial positions are above the 3000-m isobath. There is a significant enhancement of near-bottom vertical kinetic energy at frequencies higher than f in the Lagrangian spectrum, with energy levels at those frequencies being about one order of magnitude higher than those in the Eulerian spectrum (Figure 2c). At low frequencies, the energy levels in the Lagrangian spectrum become lower than the Eulerian spectrum. The reason behind this difference is that the Eulerian frame is incapable of distinguishing lee waves from the mean flow in the frequency space, and as a result the vertical kinetic energy associated with lee waves shows up at frequencies lower than f in the Eulerian spectrum.

We also calculate the rotary spectra of the horizontal velocities in the frequency space (Figure 3). In the Northern Hemisphere, the clockwise (CW) rotating component should dominate the counterclockwise (CCW) rotating component near f (Leaman & Sanford, 1975). Figure 3 shows that the rotary spectra are indeed dominated by a CW rotation centered near f within the bottom 750 m in the Lagrangian frame, whereas in the Eulerian frame the bottom energy levels of CW and CCW rotation are comparable.

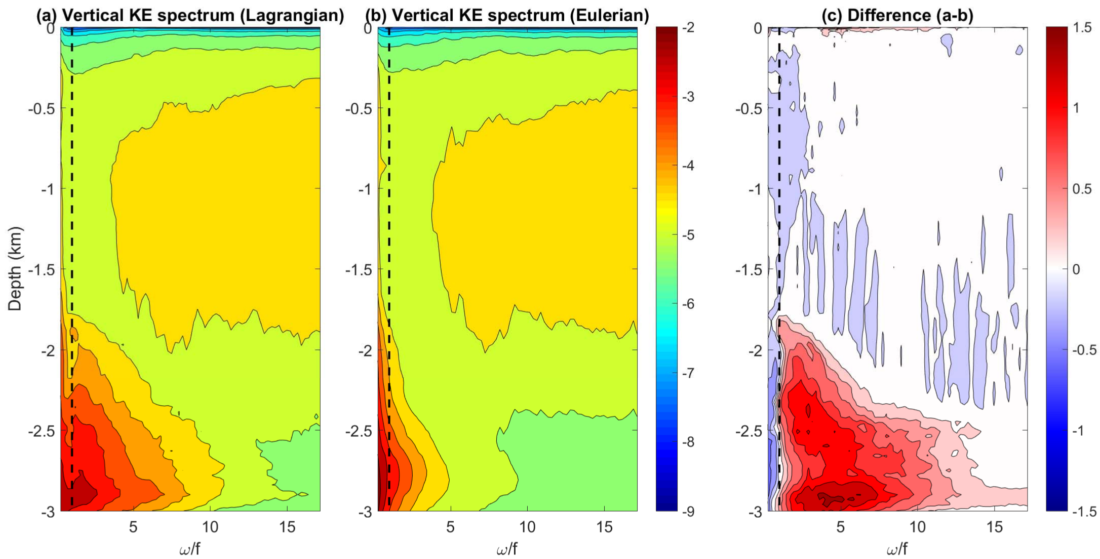

Figure 2. Horizontally-averaged vertical kinetic energy spectra in the (a) Lagrangian and (b) Eulerian frames (shading, unit: m^2/s, in log 10) and (c) their differences above the 3000-m isobath (only in the C2 region). The dashed black lines mark the inertial frequency.

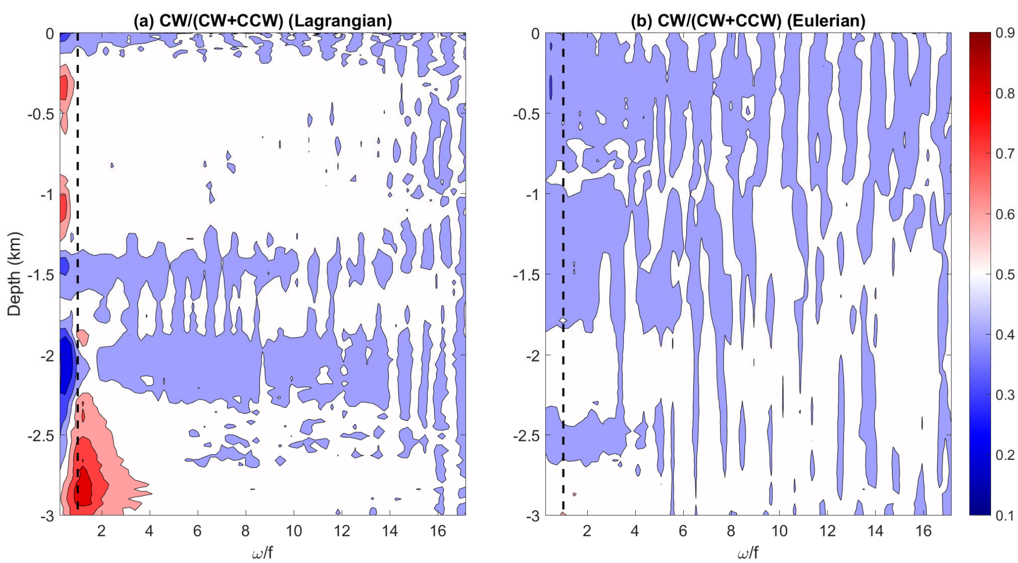

Figure 3. Horizontally-averaged rotary spectra of the horizontal velocities in the frequency space above the 3000-m isobath (shading) in the (a) Lagrangian and (b) Eulerian frame. The dashed black lines mark the inertial frequency. Red corresponds to CW dominating, while blue corresponds to CCW dominating.

2.3 Wave energy budget

Following Shakespeare and Hogg (2017), the wave energy (E_{IW}) budget can be written as:

$$\frac{\partial E_{\mathrm{IW}}}{\partial t} = -\nabla \cdot \langle \mathbf{u} E_{\mathrm{IW}} \rangle - \nabla \cdot \langle p' \mathbf{u}' \rangle + \langle \mathrm{MTWC} \rangle - \langle \varepsilon \rangle - \langle \varphi \rangle, \quad (1)$$

where angled brackets denote the time average of the middle four days. The E_{IW} consists of wave kinetic energy $E_{\mathrm{IW}}^{K}=\rho_0\left(u'^2+v'^2+w'^2\right)/2$ and wave available potential energy $E_{\mathrm{IW}}^{A}=\rho_0\left(b'^2/N^2\right)/2$, where ρ_0 is the reference density and N^2 is the background stratification. Assuming a quasi-steady wave field, the time derivative of E_{IW} can be neglected. The convergence of wave energy advection and pressure flux is dominated by their vertical components $-\langle wE_{\mathrm{IW}}\rangle_z$ and $-\langle p'w'\rangle_z$ after horizontal average over a sufficiently large area.

The energy transfer from mean flows to waves, i.e., mean-to-wave conversion (MTWC), can be calculated as:

$$\begin{aligned}\mathrm{MTWC}=&\underbrace{\rho_0\left(-w'\mathbf{u}_h'\cdot\frac{\partial\bar{\mathbf{u}}_h}{\partial z}\right)}_{\text{(i)VSH}}+\underbrace{\rho_0\left(-b'\mathbf{u}_h'\cdot\frac{\nabla_h\bar{b}}{N^2}\right)}_{\text{(ii)HBY}}+\\&\underbrace{\rho_0\left(-u'^2\cdot\frac{\partial\bar{u}}{\partial x}-v'^2\cdot\frac{\partial\bar{v}}{\partial y}\right)}_{\text{(iii)HST}}+\underbrace{\left[-\rho_0u'v'\cdot\left(\frac{\partial\bar{v}}{\partial x}+\frac{\partial\bar{u}}{\partial y}\right)\right]}_{\text{(iv)HSH}},\end{aligned}\tag{2}$$

where the four terms on the right-hand side of Eq. 2 represent in sequence the MTWC via (i) the mean vertical shear (MTWC-VSH), (ii) mean horizontal buoyancy gradient (MTWC-HBY), (iii) mean horizontal strain (MTWC-HST) and (iv) mean horizontal shear (MTWC-HSH), respectively.

The E_{IW} sink due to viscous dissipation and irreversible mixing ($D_{\mathrm{IW}}=\varepsilon+\varphi$) can be written as:

$$\varepsilon=\rho_0A_h\left[\left(\frac{\partial\mathbf{u}'}{\partial x}\right)^2+\left(\frac{\partial\mathbf{u}'}{\partial y}\right)^2\right]+\rho_0A_{4h}\left(\nabla_h^2\mathbf{u}'\right)^2+\rho_0A_z\left(\frac{\partial\mathbf{u}'}{\partial z}\right)^2,\tag{3}$$

$$\varphi=\rho_0\frac{K_{4h}}{N^2}\left(\nabla_h^2b'\right)^2+\rho_0\frac{K_z}{N^2}\left(\frac{\partial b'}{\partial z}\right)^2,\tag{4}$$

where A_h is the harmonic horizontal viscosity, A_{4h} is the bi-harmonic horizontal viscosity, A_z is the vertical viscosity. K_{4h} is the bi-harmonic horizontal diffusivity and K_z is the vertical diffusivity.

3 Results

3.1 MTWC and D_{IW}

In C2 simulation, synthetically generated small-scale (< 20 km) rough topography (with an average depth of 0 m) is added to the low-pass filtered (> 20 km) realistic topography. Here we composite E_{IW}^{K} based on the low-passed (<20 km) bathymetry (Figure 4a). The vertical profiles of E_{IW}^{K} with similar low-passed bathymetry (±15 m; i.e., the vertical interval of the composite E_{IW}^{K} is 30 m) are first horizontally averaged and then are arranged according to the low-passed bathymetry. Here we use the low-passed bathymetry as our reference bathymetry (black dashed line in Figure 4a) and regard the height above/below the low-passed bathymetry (i.e., HAB >0 or HAB<0) as the ‘trough’/‘crest’ of the small-scale topography. This composite method is more meaningful, since the 'crest' is a better representation of the 'effective topography' for lee wave generation (Baker & Mashayek, 2022). The E_{IW}^{K} is strongly bottom-enhanced especially in the shallow half of the slope region. Figure 4b shows the composited E_{IW}^{K} as a function of HAB. It peaks around HAB = 100 m and decreases to a negligible level at HAB = 500 m. Quantitatively, we find that about 90% of E_{IW}^{K} is concentrated in the region of HAB < 500 m. The E_{IW}^{A} is one or two orders of magnitude smaller than E_{IW}^{K} and is therefore negligible (not shown).

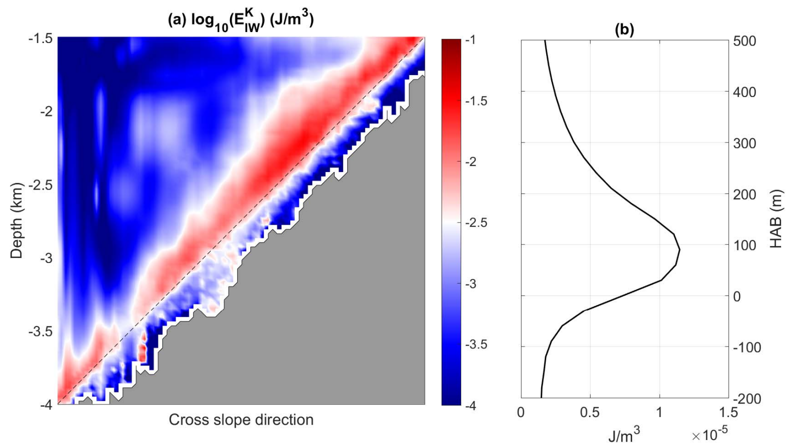

Figure 4. (a) Composited E_{IW}^{K} based on the low-pass filtered bathymetry (black dashed line). Regions without samples to compute the composite are masked by grey. (b) Composited E_{IW}^{K} as a function of HAB.

The E_{IW} can be lost via either D_{IW} or R_{IW}. To quantify their relative importance, we compute the composited E_{IW} budget as a function of HAB (Figure 5). The convergence of vertical wave pressure flux (cyan line) is negative for HAB < 100 m but is positive above, consistent with an upward lee wave pressure flux. The convergence of vertical wave energy advection (magenta line) has an opposite sign to the convergence of vertical wave pressure flux but is smaller in magnitude. As for the MTWC, the dominant terms are the MTWC-HST (red line) and MTWC-VSH (green line), both of which have large positive values for HAB ranging from -100 m to 200 m, meaning that energy is converted from mean flows to lee waves. For HAB > 200 m, the MTWC-VSH dominates the MTWC and becomes slightly negative, indicating a lee wave energy re-absorption by mean flows. The MTWC-HSH and MTWC-HBY make a negligible contribution to the MTWC (not shown). The ε (blue line) is bottom-intensified with the maximum value located at HAB = 50 m and then attenuates with the increasing HAB. The φ is small compared with other terms (not shown).

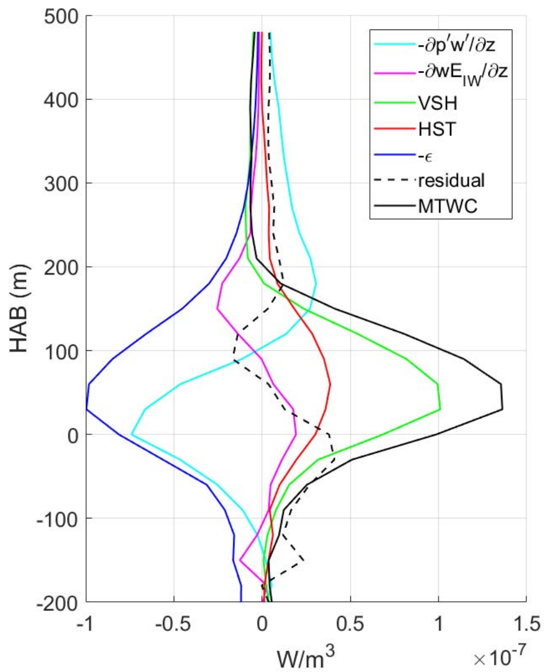

Figure 5. Composited E_{IW} budget (Eqs. 1-4) as a function of HAB. The MTWC-HSH, MTWC-HBY and φ are not shown in this figure since they make a negligible contribution to the E_{IW} budget.

Figure 6 shows the composited MTWC (Eq. 2) and D_{IW} (Eqs. 3-4). The composited method is the same as that used in Figure 4. All the terms shown in Figure 6 are concentrated right above HAB = 0 m (dashed black line). The dominant energy transfers associated with MTWC-HST and MTWC-VSH are directed from the mean flow to the lee wave field above the rough topography (positive; Figures 6a, c). Further away from the bottom, patches of negative MTWC-VSH can be found in the shallow slope region, indicating lee wave energy re-absorption by the mean flow. Compared with the magnitude of ε (Figure 6e), however, the negative values of MTWC-VSH are much weaker.

Nagai et al. (2015) estimated the contribution of R_{IW} (negative MTWC) to the total E_{IW} sink by averaging the positive and negative MTWC separately. Following Nagai et al. (2015), we first horizontally average the depth-integrated (from the sea floor to HAB = 500 m) MTWC by applying a 5 km×5 km running mean. Using running mean of different scales (5~10 km) is found to have a minor influence on the following results. We then estimate the contribution of R_{IW} to the total E_{IW} sink as:

$$R_a = \underbrace{\int \frac{\left|\{\langle \mathrm{MTWC}\rangle\}\right| - \{\langle \mathrm{MTWC}\rangle\}}{2} dA}_{R_{\mathrm{IW}}} \Big/ \underbrace{\int \frac{\left|\{\langle \mathrm{MTWC}\rangle\}\right| - \{\langle \mathrm{MTWC}\rangle\}}{2} + \{\langle D_{\mathrm{IW}}\rangle\} dA}_{\text{Total sink } (R_{\mathrm{IW}} + D_{\mathrm{IW}})} \quad , (5)$$

where the braces represent the integration from the sea floor to HAB = 500 m, $|\cdot|$ represents the absolute value and $\int dA$ denotes the horizontal integration. The first integral term on the right hand of Eq. 5 represents the depth-integrated energy sink associated with negative MTWC (i.e., R_{IW}) and the second integral term represents the total wave energy sink (i.e., $R_{IW}+D_{IW}$).

The value of R_a is found to be about 5%. This suggests that D_{IW} is the dominant sink of E_{IW} in our experiment, with R_{IW} being of little importance. Figure 7 shows R_a as a function of the depth of the low-pass filtered (>20km) bathymetry at an interval of 500 m. The value of R_a ranges from 2% to 8%, being larger in shallower regions. This is due to the negative MTWC-VSH band in the shallow half of the slope region (Figure 6a). Even there, R_{IW} still only accounts for a small percentage of the total E_{IW} sink.

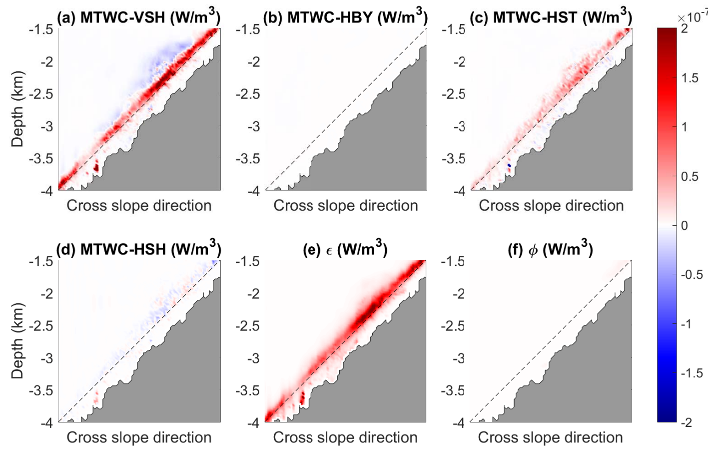

Figure 6. Distribution of composited (a) MTWC-VSH, (b) MTWC-HBY, (c) MTWC-HST, (d) MTWC-HSH, (e) ε and (f) φ based on the low-pass filtered bathymetry (the dashed black line).

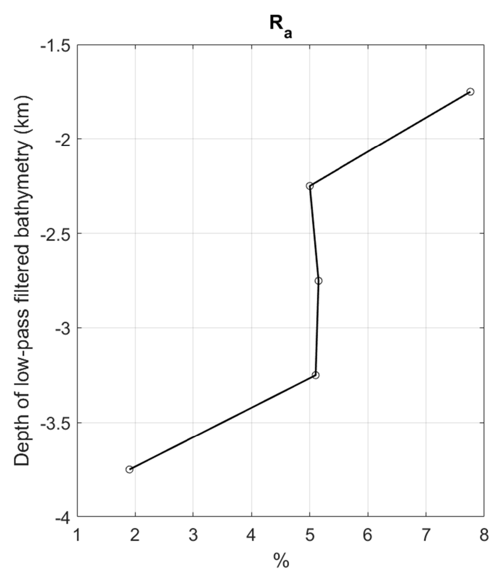

Figure 7. The average R_a as a function of the depth of the low-pass filtered bathymetry.

Given the large positive MTWC, it is meaningful to assess the relative importance between the energy extracted from mean flows due to lee wave generation at the sea floor and that due to MTWC during the subsequent upward radiation of lee waves. To do that, we compare the vertical lee wave pressure flux at the sea floor (i.e., $\langle p_b' w_b' \rangle$, the subscript '*b*' indicates values of the bottom-most cells) with the depth-integrated wave dissipation $\{\langle D_{\mathrm{IW}} \rangle\}$ that is almost entirely attributed to $\{\langle \varepsilon \rangle\}$. The value of $\{\langle D_{\mathrm{IW}} \rangle\}$ is 2.32×10^{-5} W/m^2, about three times of 0.77×10^{-5} W/m^2 for $\langle p_b' w_b' \rangle$. The remaining two thirds of $\{\langle D_{\mathrm{IW}} \rangle\}$ is largely balanced by the depth-integrated $\langle \mathrm{MTWC} \rangle$ (1.24×10^{-5} W/m^2). In other words, lee waves extract energy from mean flows not only when they are generated at the rough topography but also during their subsequent upward radiation primarily via MTWC-VSH and MTWC-HST of mean flows. This finding has important implications for the role of lee waves in the ocean energy budget and for the parameterization of the effect of lee waves in ocean models.

3.2 Potential mechanisms for MTWC

Energy is transferred from mean flows to lee waves primarily through MTWC-VSH and MTWC-HST. The former can be understood based on the conservation of wave action (Kunze & Lien, 2019). When the mean flow speed decreases towards the sea floor, the wave intrinsic frequency increases as lee waves radiate upwards, causing a positive MTWC-VSH to conserve the wave action, and vice versa. This mechanism is further confirmed by the positive correlation between the normalized vertical shear of mean flow speed and MTWC-VSH (Figure 8a). In the northern SCS, the mean flow speed first increases with HAB until it reaches the maximum value at HAB = 250 m, and decreases further above (Figure 8b). This vertical distribution of mean flow speed is generally consistent with MTWC-VSH which has relatively large positive values at depths between HAB = -100 m and HAB = 200 m and negative values above HAB = 200 m.

Several mechanisms are potentially responsible for the positive MTWC-HST, including the wave capture (Bühler & McIntyre, 2005; Jing et al. 2018), anticyclonic-ageostrophic instability (AAI; Molemaker et al., 2005), and relaxation effect (Müller, 1976). For the wave capture mechanism, a unidirectional energy transfer from mean flows to waves only occurs when the Okubo-Weiss (OW; Provenzale, 1999) parameter is positive (Bühler & McIntyre, 2005), where $\mathrm{OW} = S_n{}^2 + S_s{}^2 - \xi^2$ with $S_n = (\frac{\partial \bar{u}}{\partial x} - \frac{\partial \bar{v}}{\partial y})$ the normal strain, $S_s = (\frac{\partial \bar{v}}{\partial x} + \frac{\partial \bar{u}}{\partial y})$ the shear strain, and $\xi = \frac{\partial \bar{v}}{\partial x} - \frac{\partial \bar{u}}{\partial y}$ the relative vorticity. However, MTWC-HST is found to be insensitive to the sign of OW parameter within HAB = 0-300 m over the northern SCS. Its composited mean value is even larger in case of OW < 0 (1.82×10^{-8} W/m^3) than OW > 0 (1.30×10^{-8} W/m^3), suggesting that the wave capture mechanism is unlikely to make an important contribution to MTWC-HST (Figure 9a, b). This may be related to the fact that the horizontal scale of bottom mean flows is significantly reduced in the presence of rough topography and as a result they become less effective in wave capturing.

AAI occurs when $f+\xi-|S|<0$ ($S=\sqrt{S_n^2+S_s^2}$ is the horizontal strain rate) causing the mean flow to lose balance and promoting the energy transfer from mean flows to waves via MTWC-HST. Previous studies (e.g., Yang et al., 2021; Yang et al., 2022) reveal that the enhanced wave dissipation above the rough topography is accompanied by AAI. In our simulation, we find that the composited mean MTWC-HST within HAB = 0-300 m is more than an order of larger when AAI occurs (3.51×10^{-7} W/m^3) than otherwise (9.29×10^{-9} W/m^3) (Figure 9c, d). Therefore, although the probability of occurrence of AAI is only 2.1% within HAB = 0-300 m, it contributes to 45% volume integrated MTWC-HST. Combined with the findings of (Yang et al., 2021; Yang et al., 2022), our analysis suggests that AAI provides an efficient energy dissipation pathway. The remaining half of MTWC-HST might be partially attributed to the relaxation effect, which always induces a unidirectional energy transfer from mean flows to waves regardless (Müller, 1976). However, its contribution is difficult to be quantified and will not be pursued in this study.

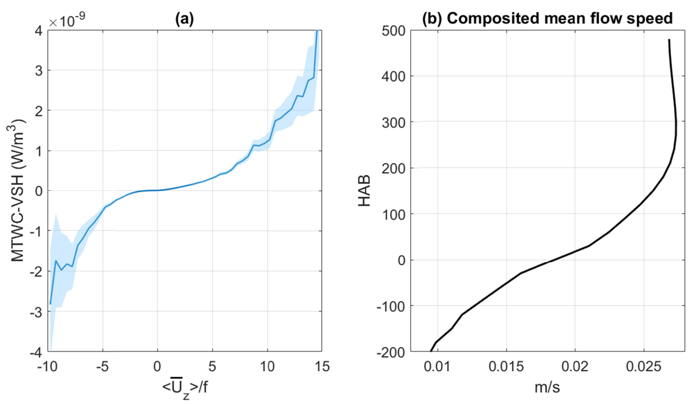

Figure 8. (a) The relationship between the normalized vertical shear of mean flow speed and MTWC-VSH. Blue shading represents the 95% confidence intervals. (b) Composited mean flow speed as function of HAB.

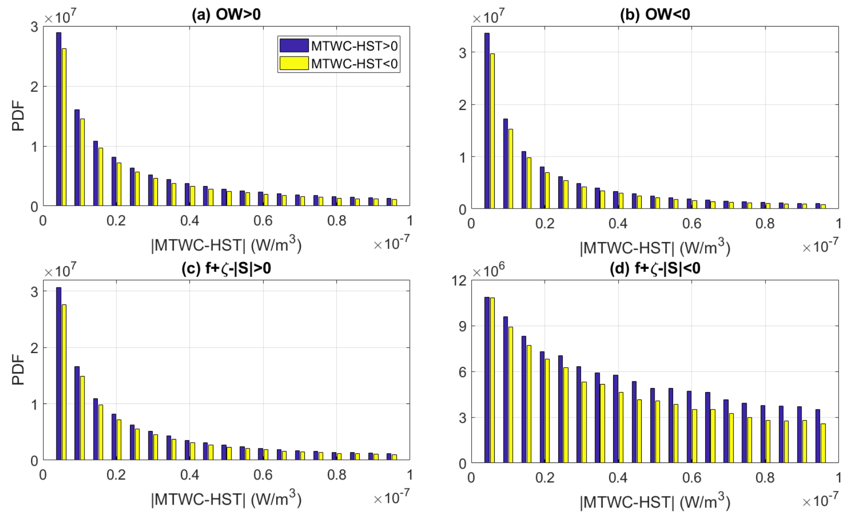

Figure 9. Probability density distributions (PDFs) of MTWC-HST under the case of (a) OW>0 and (b) OW<0, respectively. PDFs of MTWC-HST under the case of (c) $f+\xi-|S|<0$ and (d) $f+\xi-|S|>0$, respectively.

4 Discussion

Our results show that wave dissipation (D_{IW}) is the dominant sink of wave energy (E_{IW}) in the northern SCS, with wave energy re-absorption by mean flows (R_{IW}) being of secondary importance. The value of re-absorption fraction (R_a) ranges from 2% to 8%, with an average value of 5%, much smaller than the re-absorption limit (~50% for the northern SCS parameters) estimated by Kunze and Lien (2019) who assumed that there is no D_{IW} before wave re-absorption by mean flows. Several mechanisms could account for this evident discrepancy.

First, the vertical structure of near-bottom mean flow in the northern SCS favors energy transfer from mean flows to waves via MTWC-VSH (Figure 8b). This energy transfer from mean flows to waves is further augmented via positive MTWC-HST (Figure 5; Figure 6). To assess the important effect of MTWC on R_a , we estimate R_a along a selected section used in the case study of Yang et al. (2022) where the mean flow speed is almost uniform within several hundreds of meters above the sea floor and becomes weaker further above (Figure 10). This favors energy transfer from waves to mean flows through MTWC-VSH. In addition, we find that MTWC is mainly ascribed to MTWC-VSH for this selected section with MTWC-HST making negligible contribution. Accordingly, MTWC is negative, corresponding to an energy transfer from waves to mean flows. However, even in this case, the value of R_a is only 10-15%, which is still far less than the re-absorption limit estimated by Kunze and Lien (2019), suggesting that MTWC alone cannot entirely account for the small R_a in the northern SCS.

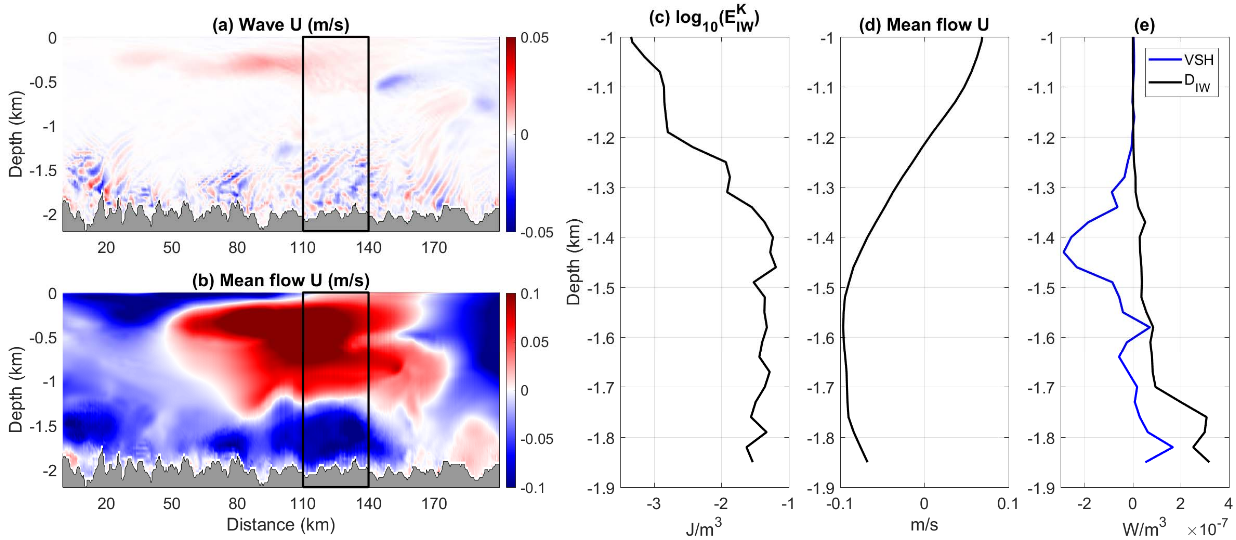

Figure 10. A selected section of zonal wave and mean flow velocities in the case study of Yang et al. (2022). The section-averaged (black box in a & b) E_{IW}^{K}, zonal mean flow velocity and MTWC-VSH and D_{IW} are shown in (c), (d) and (e). The meridional mean flow velocity is much weaker than the zonal component and negligible.

Second, the D_{IW} is tightly related to the value of Fr. For example, in idealized experiments representative of the Southern Ocean, Nikurashin and Ferrari (2010a) found 50% of E_{IW} dissipated in the bottom 1 km for $Fr > 0.5$ but only 10% for $Fr = 0.2$. In our realistic simulation of the northern SCS, Fr is generally larger than one due to the weak bottom mean flow. This indicates that lee waves generated in the northern SCS tend to dissipate close to the rough topography and consequently they are less likely to interact with mean flows. In the following, we will discuss the potential mechanisms responsible for the small R_a in the northern SCS with a particular focus on the sensitivity to the vertical structure of mean flows and Fr.

We conduct five idealized simulations (Figure 11). All the idealized experiments are 2-D and non-hydrostatic with a horizontal resolution of 10 m and a vertical resolution of 5 m in the bottom 2 km. Explicit viscosity and diffusivity are set to 10^{-5} m^2/s to avoid excessive D_{IW} (Shakespeare & Hogg, 2017). The model domain is 28 km long and 7.1 km deep. The wave momentum and buoyancy are absorbed with a sponge layer above HAB = 2 km so that the artificial upper bound of the domain does not affect the solution. A uniform Coriolis frequency of $f = 5 \times 10^{-5}$ s^{-1} and stratification of $N = 2 \times 10^{-3}$ s^{-1} are used. The bathymetry used for the idealized simulations is a stochastic version of the bathymetric spectrum consisting of wavenumbers between f/U_b and N/U_b (Goff & Jordan, 1988).

In the first experiment (Case 1), a vertical uniform body force is applied in the y-momentum equation equal to fU_0 (Nikurashin et al., 2014). Similar to the bottom mean flow observed in the selected section (Figure 10), we set $U_0 = 0.1$ m/s. In the following three experiments, the body forces with the bottom 400 m are the same as Case 1 and then decrease linearly with height until $U_0 = 0$ m/s at HAB = 800 m. The normalized vertical shear of mean flows, i.e., U_{0z}/f is -5 for HAB = 400-800 m. The only difference among these three experiments is Fr by varying the root-mean-squared height h of the synthetic topography. Case 2 has the same Fr (0.9) as case 1 and the other two experiments (Case 3 and 4) have smaller values of Fr (0.45 and 0.18, respectively). In the last experiment (Case 5) the bottom mean flow velocity increases with height for HAB = 0-400 m, with a normalized shear of $U_{0z}/f = 1$ (similar to the bottom mean flow structure in the realistic model; Figure 8b) at HAB = 0-400 m. Above HAB = 400 m, it has same mean flow structure as Cases 2-4. The Fr of Case 5 is 0.18 (note h and U_b in Case 5 are different from Case 4). All the experiments are run for 10 days and they generally reach an equilibrium state after 5 days or so. The last two inertial periods (70 hours) are used for analysis.

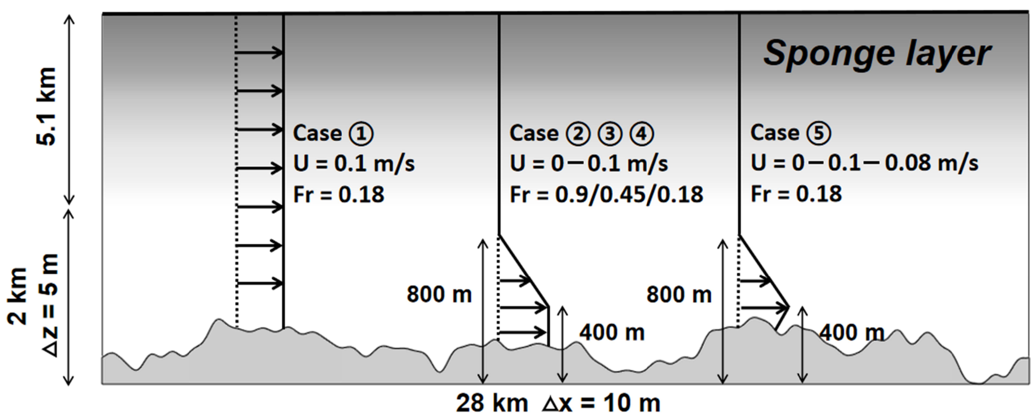

Figure 11. Schematic of the idealized model setup. The grey shading in the upper 5.1 km of the domain indicates the sponge layer.

Following Nikurashin et al. (2014), the model results are decomposed into the mean flow and wave components as,

$$\mathbf{u} = \mathbf{U}_0 + \mathbf{u}', \; p = P_0 + p', \; b = b_0 + b', \tag{6}$$

where $\mathbf{U_0} = (U_0, 0, 0)$, P_0 and b_0 are the velocity, pressure and buoyancy associated with mean flows. The value of b_0 is derived from the prescribed background stratification. Once b_0 is obtained, P_0 is derived from the hydrostatic approximation.

To the leading order, the divergence of lee wave pressure flux is balanced by the MTWC through the Eliassen-Palm (E-P) flux (Eliassen & Palm, 1960) and D_{IW} (Baker & Mashayek, 2021), i.e.,

$$-\langle wE_{\mathrm{IW}}\rangle_z - \langle p'w'\rangle_z - U_{0z}\langle F\rangle - \langle D_{\mathrm{IW}}\rangle = 0, \tag{7}$$

where $F = \rho_0 u'w' - \dfrac{\rho_0 f v'b'}{N^2}$ is the E-P flux. Note the third term on the left-hand side ($-U_{0z}\langle F\rangle$) can be regard as the MTWC, since the remaining terms with y-derivatives (e.g., MTWC-HST and MTWC-HSH) are zero in the 2-D simulations.

In the limit of sub-critical topography (i.e., $Fr < 0.7$; Nikurashin & Ferrari, 2010a), the linear theory (Bell, 1975a, b) predicts the wave pressure flux $\langle p'w' \rangle$ as:

$$E_{Bell} = \frac{\rho_0}{4\pi^2}\int_{-\infty}^{+\infty}\int_{-\infty}^{+\infty} P(k,l)\frac{(\mathbf{U}_b\cdot\mathbf{k})}{|\mathbf{k}|}\sqrt{N^2-(\mathbf{U}_b\cdot\mathbf{k})^2}\cdot\sqrt{(\mathbf{U}_b\cdot\mathbf{k})^2-f^2}\,dkdl\,, \quad (8)$$

where $P(k,l)=\dfrac{2\pi H^2(\mu-2)}{k_0 l_0}\left(1+\dfrac{k^2}{k_0^{\,2}}+\dfrac{l^2}{l_0^{\,2}}\right)^{-\mu/2}$ is the 2-D topography spectrum, H^2 is the variance of the full topographic height, (k_0, l_0) are the characteristic wavenumbers of the principal axes of anisotropy, $\mathbf{k} = (k, l)$ is the wavenumber vector and μ is the high-wavenumber roll-off slope.

For an isotropic topography spectrum (i.e., $k_0 = l_0$) and wavenumbers of the radiating waves $|\mathbf{k}|^2 >> k_0^{\,2}$, E_{Bell} in (8) can be simplified as (Nikurashin & Ferrari, 2010b):

$$E_{Bell} = \frac{\rho_0|\mathbf{U}_b|^3}{\pi^2}\int_{f/|\mathbf{U}_b|}^{N/|\mathbf{U}_b|} kP_{eff}(k)m(k)\left(1-\frac{f^2}{|\mathbf{U}_b|^2k^2}\right)dk\,, \quad (9)$$

where $m(k)=k\sqrt{\dfrac{N^2-|\mathbf{U}_b|k^2}{|\mathbf{U}_b|k^2-f^2}}$ is the vertical wavenumber and

$P_{eff}(k)=H^2k_0^{\,\mu-2}(\mu-2)B\left(\dfrac{1}{2},\dfrac{\mu}{2}\right)k^{1-\mu}$ is the effective 1-D topography spectrum (B is the beta function). In our idealized experiments, $H = 78$ m, $k_0 = 3.4 \times 10^{-4}$ m^{-1} and $\mu = 3.2$. Finally, to account for topography blocking and pressure flux saturation in the large Fr situation, E_{Bell} in (9) is multiplied by $(0.7/Fr)^2$ when $Fr > 0.7$.

4.1 Lee wave energetics with and without mean flow shear

In this subsection, we examine the effect of vertical shear of mean flows on R_a by focusing on the results of the first two experiments.

Figure 12 shows the snapshots of the zonal wave velocity and wave dissipation in the first two experiments. In the first experiment with uniform U_0, the wave field is clearly visible throughout the bottom 2 km (Figure 12a). When the vertical shear is added to the mean flow in Case 2, the wave field below 400 m remains similar to that in Case 1. However, as the waves radiate upward into the shear zone (HAB = 400-800 m), the wave amplitudes decrease quickly with height, indicating a sink of E_{IW} due possibly to R_{IW} at the critical layer (Kunze & Lien, 2019). The reduction in E_{IW} in Case 2 can also be seen from the horizontally averaged E_{IW} profile, which shows a rapid reduction from HAB = 400 m to 800 m (Figures 13a). In the idealized simulations with bottom-up decreasing mean flows and monochromatic topography, Sun et al. (2022) report that the wave amplitudes first enhance with HAB and then sharply drop to zero as the waves approach the critical layer. Here we do not observe the enhancement of wave amplitudes, which may be due to the use of multichromatic topography in our study. Lee waves generated above the multichromatic topography have a range of intrinsic frequencies spanning from f to N. Waves with frequencies close to f meet their critical layers earlier and drop their amplitudes rapidly which could counteract the enhancement of higher frequency waves (H. Sun, personal communication). In addition, the wave vertical wavelengths become smaller as the waves radiate upwards, consistent with the behaviors of waves approaching the critical layer (Figure 12b). The relationship between the vertical wavenumber of lee waves and the mean flow shear can be written as: $\frac{\partial m}{\partial z} = -kU_{0z} / \frac{\partial \omega}{\partial m}$ (ω is the wave intrinsic frequency; Sun et al., 2022). Therefore, for waves radiating upward through a mean flow with negative vertical shear, their vertical wavenumbers (wavelengths) increase (decrease) with HAB until the waves reach the critical layer where the vertical wavenumbers $m \rightarrow \infty$, creating sharp vertical shear of wave current and resulting in enhanced D_{IW} (Wurtele, 1996). The reduced wavelengths could lead to enhanced D_{IW} through the vertical shear instability even before they reach the critical layer (Sun et al., 2022). This enhanced D_{IW} can be also seen in Figures 12c, d and Figure 13c. Although the E_{IW} in Case 2 is significantly reduced between 400 m and 800 m (Figures 12a, b; Figure 13a), there is no obvious difference in wave dissipation between Case 1 and Case 2 (Figures 12c, d; Figure 13c). In addition, the horizontally averaged vertical wave pressure flux is also largely reduced from HAB = 400 m to 800 m in Case 2 (Figure 13b), suggesting that MTWC through E-P flux is responsible for the reduction of vertical wave pressure flux seen in Case 2.

We also estimate the vertical wave pressure flux predicted by the linear theory (Eq. 9; Figure 13b). Here we use the stratification at the maximum wave pressure flux (HAB = 200 m) instead of the initial stratification, since we find a reduction of stratification close to the topography in all simulations. The wave pressure flux predicted by the linear theory is slightly weaker than the maximum wave pressure flux simulated in Case 1 and Case 2, which may be because the pressure anomaly defined in Eq. 6 also includes the contribution of other nonwave motions such as hydraulic jumps (e.g., Baines, 1995) and topographical blocking flows (e.g., Klymak, 2018). Figures 14a, b show the wave energy budgets for Cases 1 and 2. In these large Fr ($Fr = 0.9$) simulations, $\langle p'w' \rangle_z$ is generally balanced by -$\langle D_{\mathrm{IW}} \rangle$ and -$\langle wE_{\mathrm{IW}} \rangle_z$, with $-U_{0z}\langle F \rangle$ only making a negligible contribution.

To quantify the contribution of MTWC to the reduction of wave pressure flux in the shear zone of the mean flows, we integrate Eq. 7 over the entire shear zone (here we don't consider the $\langle wE_{\mathrm{IW}} \rangle_z$ term, since it is negligible above HAB = 400 m), i.e.,

$$\langle p'w' \rangle\big|_{HAB=400\,\mathrm{m}} - \langle p'w' \rangle\big|_{HAB=800\,\mathrm{m}} = \int_{400\,\mathrm{m}}^{800\,\mathrm{m}} U_{0z}\langle F \rangle + \langle D_{\mathrm{IW}} \rangle dz \,. \tag{10}$$

Table 1 shows the horizontally averaged each term in Eq. 10. The reduction of wave pressure flux is doubled in Case 2 in the shear zone, with comparable contributions from the energy exchange term and dissipation term. This indicates R_{IW} is a non-negligible route for E_{IW} sink in the shear zone of mean flows in Case 2. As a result, the wave field above HAB = 800 m is significantly weaker in Case 2 than Case 1 (Figure 12b).

We measure the ratio of R_{IW} to the total E_{IW} sink using two indices. The first index is identical to R_a except that the vertical integration for MTWC and D_{IW} is performed over HAB = 0-800 m. As the bottom wave dissipation may be overestimated due to the contribution of topographical blocking flows, the second index is computed as the ratio of vertically integrated MTWC to the wave pressure flux predicted by the linear theory. The two indices produce very similar results for Case 2 (Table 2) and are close to our realistic model result (10-15%). In Case 2, most of E_{IW} is dissipated close to the bottom (Figures 12d; Figure 13c), leaving only a small percentage (~20%) of E_{IW} radiating upwards into the ocean interior that can be potentially re-absorbed by mean flows. This results in the relatively small re-absorption fraction both in the idealized and realistic models.

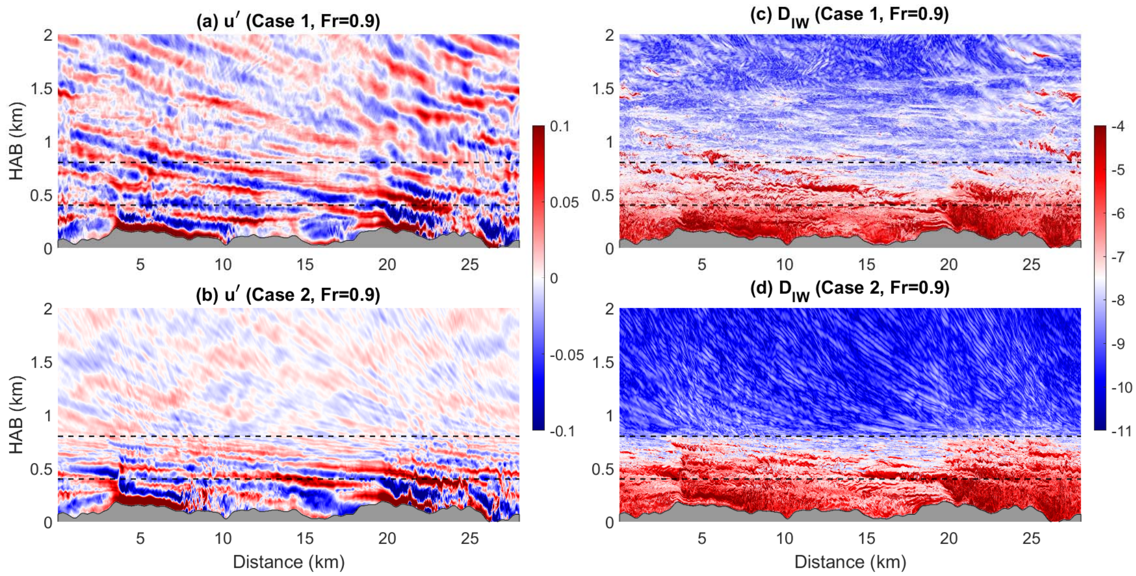

Figure 12. Snapshots of the u' (a-b; m/s) and D_{IW} (c-d; W/m^3; in log 10) in the first two cases.

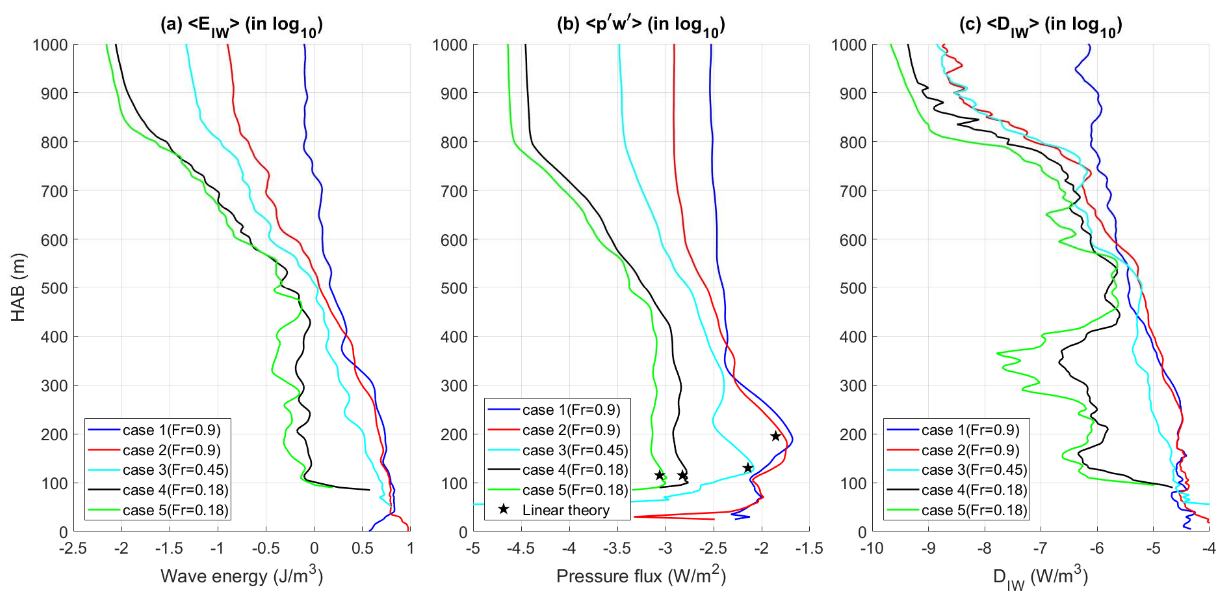

Figure 13. Horizontal-averaged (a) E_{IW}, (b) wave pressure flux and (c) D_{IW} in Cases 1-5. All in $\log_{10}$.

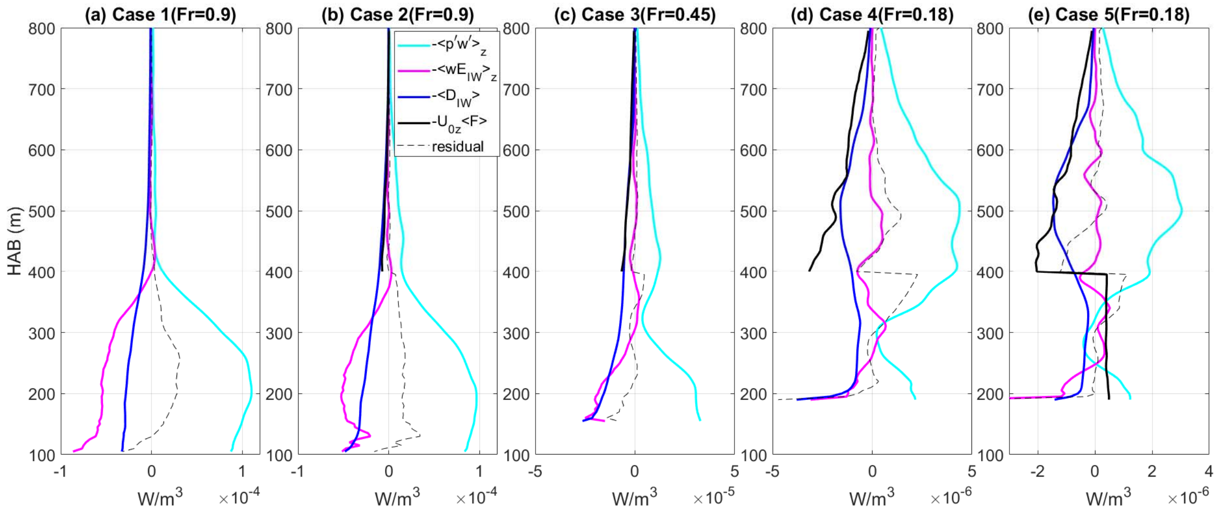

Figure 14. Wave energy budgets in Cases 1-5. The $-\langle wE_{\mathrm{IW}}\rangle_z$, $-\langle p'w'\rangle_z$ and $-\langle D_{\mathrm{IW}}\rangle$ are smoothed over a typical vertical wavelength (150 m) of IOs. Note scales for *x*-axes are different in each subplot.

Table 1. Depth-integration of (7) over the entire height of the shear flow (HAB = 400-800 m). Unit: mW/m^2.

Experiments	$-\int\langle p'w'\rangle_z dz$	$\int U_{0z}\langle F\rangle dz$	$\int\langle D_{\mathrm{IW}}\rangle dz$
Case 1 (*Fr* = 0.9)	1.3	0	1.2
Case 2 (*Fr* = 0.9)	2.6	1.1	1.4
Case 3 (*Fr* = 0.45)	2.2	1.1	1.0
Case 4 (*Fr* = 0.18)	1.1	0.6	0.4
Case 5 (*Fr* = 0.18)	0.8	0.4	0.3

Table 2. Wave energy absorption fractions in Cases 2-5.

Experiments	Index 1	Index 2
Case 2 (*Fr* = 0.9)	8%	7%
Case 3 (*Fr* = 0.45)	16%	14%
Case 4 (*Fr* = 0.18)	39%	39%
Case 5 (*Fr* = 0.18)	33%	34%

4.2 Sensitivity to *Fr*

Figure 15 shows the snapshots of the zonal wave velocity and wave dissipation in Case 3 and Case 4. The smaller values of *Fr* (compared to Case 2) in these two experiments lead to smaller wave amplitudes and wave dissipation. In addition, different from the large *Fr* simulation (Case 2), the contribution of $-\langle D_{\mathrm{IW}} \rangle$ and $-U_{0z}\langle F \rangle$ to $\langle p'w' \rangle_z$ is comparable, with $\langle wE_{\mathrm{IW}} \rangle_z$ only making a negligible contribution (Figure 14c, d). Similar to Case 2, the E_{IW} in Case 3 and Case 4 also decreases sharply in the shear zone of mean flows for HAB = 400-800 m.

Nikurashin and Ferrari (2010a) classified three regimes according to the values of *Fr*. The first regime ($Fr < 0.3$; Case 4) is characterized by stationary lee wave generation and the growth of inertial oscillations (IOs) do not significantly modify the wave generation process. In Case 4, the bottom wave dissipation is much weaker compared to Case 2 and Case 3. Relatively large wave dissipation can only be found very close to the topography (Figure 13c; Figure 15d), which results in weak attenuation of E_{IW} and pressure flux below HAB = 400 m (Figures 13a, b). Significant wave dissipation mainly occurs in the shear zone (HAB = 400-800 m) due to shear instability caused by the reduced vertical wavelengths (Table 1; Figure 13c; Figure 15d). To quantify shear instability in the shear zone, we calculate the Richardson number ($\mathrm{Ri} = N^2/\mathbf{u}_z^2$; Figure 16). The Ri is mostly greater than 0.25, corresponding to a stable condition. Areas of small Ri are generally found to be consistent with the distribution of enhanced D_{IW}. It should be noted that the vertical shear of mean flows is much smaller compared with N^2 and thus makes a negligible contribution to the reduced Ri. The re-absorption fraction in Case 4 is quite large (Table 2) and is close to the re-absorption limit estimated by Kunze and Lien (2019) who assumed that there is no D_{IW} before their re-absorption by mean flows. The second regime (Fr = 0.3-0.7; Case 3) develops with the generation of inertial frequency harmonics. In this regime, the rapid growth of IOs could significantly modify the wave vertical scales and promote wave breaking (Nikurashin & Ferrari, 2010a; Zemskova & Grisouard, 2021). The growth of IOs dissipates a significant amount of E_{IW} below HAB = 400 m (Figure 13c; Figure 15c), and leaves only about one third of the E_{IW} radiating into the shear zone. Even though the wave re-absorption fraction in Case 3 is greater than that in Case 2, the R_{IW} is still of secondary importance to the total E_{IW} sink (Table 2). The last regime ($Fr > 0.7$) is characterized by a saturation of the wave pressure flux that no longer increases with *Fr* and has been discussed in Case 2.

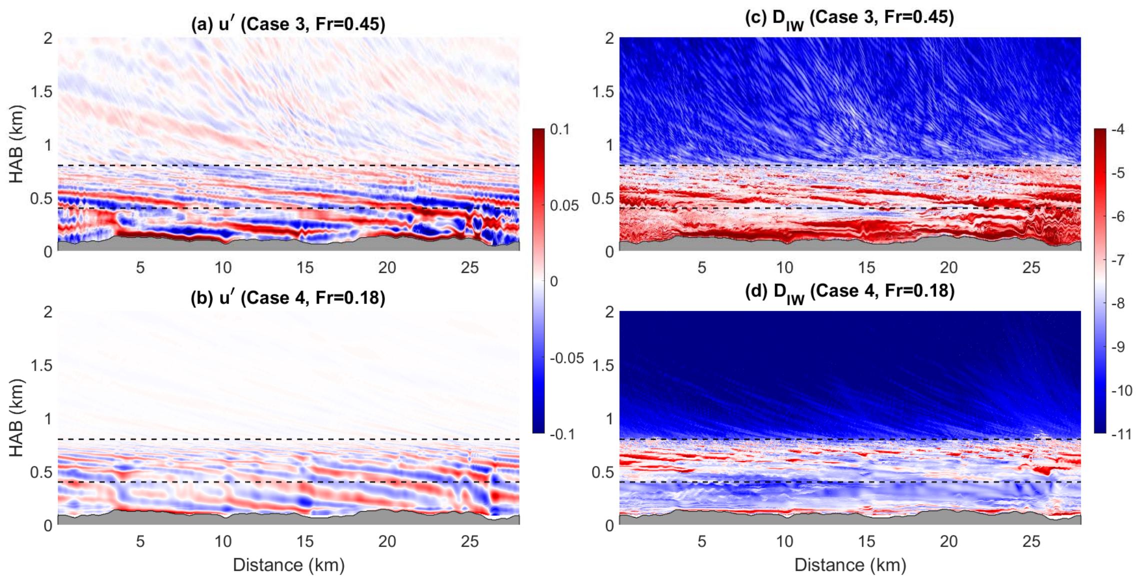

Figure 15. Same as Figure 12, but for Case 3 and Case 4.

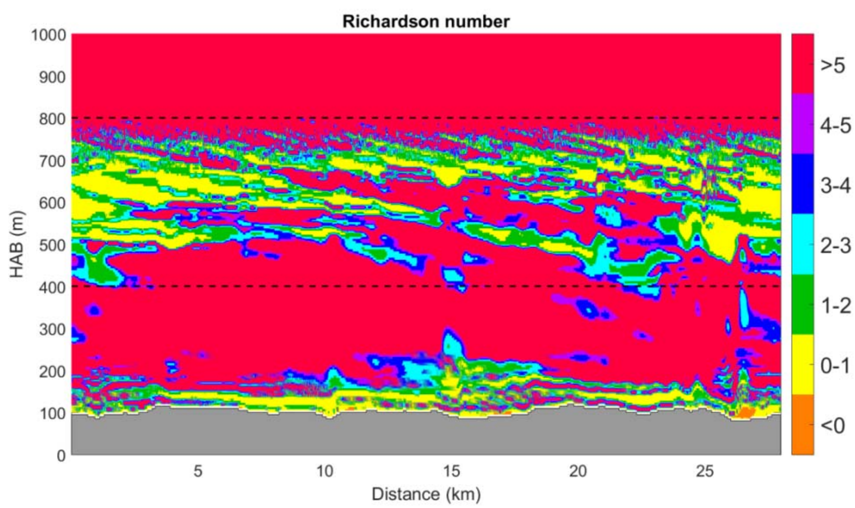

Figure 16. Snapshot of Ri in Case 4.

4.3 Sensitivity to mean flow structure

Motivated by the composited mean flow structure in the realistic model (Figure 8b), we conduct experiment Case 5 initialized with a near-bottom mean flow velocity profile that increases with height. This increase of mean flow velocity with height favors energy transfer from mean flows to waves, rather than R_{IW}, and may contribute to the small re-absorption fraction found in the northern SCS.

The results of Case 5 are very similar to Case 4. For example, the wave energy and pressure flux in Case 5 are only slightly smaller than those in Case 4 and the wave dissipation is also enhanced at HAB = 400-800 m (Figure 13). In Case 5, the pressure flux reduces by about 20% (1 mW/m^2 → 0.8 mW/m^2) from the bottom to HAB = 400 m, which is somewhat less than the 30%

reduction found in Case 4 (1.7 mW/m^2 → 1.2 mW/m^2), due possibly to energy transfer from the positively sheared near-bottom mean flow to the wave field. The vertically integrated energy transfer from mean flows to waves below HAB = 400 m is 0.12 mW/m^2 compared to 0.42 mW/m^2 from waves to mean flows at HAB = 400-800 m (Table 1), resulting a net R_{IW} of 0.3 mW/m^2. Even though the wave re-absorption fraction in Case 5 is slightly smaller than that in Case 4 (Table 2), the R_{IW} is still a non-negligible route to the total E_{IW} sink. Our result thus suggests that the small R_a in the northern SCS is primarily due to the large *Fr* (larger than one) there and, to a lesser extent, to the vertical structure of bottom mean flows.

4.4 Potential mechanisms for small re-absorption fraction in northern SCS

Our realistic simulations indicate that R_{IW} is not an important sink for lee waves in the northern SCS. Several mechanisms could contribute to this result. Firstly, the vertical structure of the near-bottom flow field favors energy transfer from mean flows to waves, rather than R_{IW}. Secondly, there is also a permanent energy transfer from mean flows to waves associated with the horizontal strain of mean flows. This result also suggests that the role of lee waves in ocean energy dissipation and mixing may have been underestimated, since wave-mean flow energy exchanges have not yet been considered in the existing estimates of E_{IW} conversion rates (e.g., Nikurashin & Ferrari, 2011; Scott et al., 2011; Wright et al., 2014). In addition, as indicated by our idealized simulations, the re-absorption fraction decrease with increasing *Fr*. In our realistic simulation of the northern SCS, *Fr* is generally larger than one due to the weak bottom velocity. So we would expect a small re-absorption fraction in the northern SCS. Small *Fr* can be found in regions of the Southern Ocean where topographic variance is small and bottom velocity is large (Nikurashin & Ferrari, 2011), suggesting that wave re-absorption could be an important route to E_{IW} sink there. Finally, D_{IW} tends to be enhanced under a negatively sheared mean flow due to the reduction of vertical wavelengths as the waves propagate upwards. This enhanced D_{IW} occurs even before the waves reach the critical layer (Sun et al., 2022), and consequently there is less E_{IW} left to be re-absorbed by mean flows.

5 Summary

The sink of lee waves generated in the northern SCS is investigated in a high-resolution nested model initialized with a synthetically-generated rough topography. A Lagrangian filtering technique is adapted to decompose the ocean currents into wave and mean flow components. Our results show that the wave energy dissipation is the dominant sink of lee wave energy in the northern SCS, with wave energy re-absorption by the mean flows ($R_a = 2-8\%$) being of secondary importance.

The dominant direction of energy transfer is from mean flows to lee waves through the vertical shear (MTWC-VSH) and horizontal strain (MTWC-HST) of mean flows. The positive MTWC-VSH is mainly ascribed to the increase of mean flow speed with the increasing height above the sea floor. The anticyclonic-ageostrophic instability (AAI) that could cause the mean flow to lose balance contributes importantly to the positive MTWC-HST.

A series of idealized experiments are conducted to understand the weak wave energy re-absorption by mean flows in the northern SCS. It is found that the small R_a in the northern SCS is primarily ascribed to the large *Fr* (larger than one) and, to a lesser extent, the vertical structure of bottom mean flows. Wave energy re-absorption is found to be important for the small *Fr* (< 0.3) regime. In this regime, lee wave energy dissipation near the bottom topography is relatively small, which leaves a large amount of wave energy radiating upwards to interact with the mean flows. As a result, the value of R_a in the small *Fr* regime is close to the re-absorption limit estimated by Kunze and Lien (2019) who assumed that there is no wave energy dissipation before their re-absorption by the mean flow.

Our study mainly focuses on the energy exchange between the mean flow and lee waves. Recent studies (e.g., Cusack et al, 2020; Shakespeare and Hogg, 2017; Zemskova & Grisouard, 2022) found the energy exchange between the mean flow/lee waves and other higher frequency internal waves could also be a potential route for lee wave energy sink. Further studies are therefore required to improve our understanding of the role of wave-wave interaction in the lee wave energy sink.

Acknowledgments

ZY and ZJ are supported by Taishan Scholar Funds (tsqn201909052), Qingdao applied research project. ZY thanks H. Sun for her helpful discussions. The research presented in this paper was carried out on the High Performance Computing Cluster supported by National Supercomputer Center in Tianjin. We thank two anonymous reviewers for their helpful comments that led to significant improvement of this manuscript.

Data availability statement

The model configuration files and snapshots are available online (https://doi.org/10.7910/DVN/M2QSGG).

References

Baines, P. G. (1995). Topographic effects in stratified flows. Cambridge Press

Baker, L. E., & Mashayek, A. (2021). Surface reflection of bottom generated oceanic lee waves. *Journal of Fluid Mechanics*, 924(Bell 1975), 1–34. https://doi.org/10.1017/jfm.2021.627

Baker, L. E., & Mashayek, A. (2022). The impact of realistic topographic representation of the parameterisation of lee wave energy flux. *Journal of Geophysical Research: Oceans*, 127, e2022JC018995. https://doi.org/10.1029/2022JC018995

Becker, J., Sandwell, D., Smith, W., Braud, J., Binder, B., Depner, J., et al. (2009). Global bathymetry and elevation data at 30 arc seconds resolution: SRTM30_PLUS. *Marine Geodesy*, 32(4), 355–371. https://doi.org/10.1080/01490410903297766

Bell, T. H. (1975a). Lee waves in stratified flows with simple harmonic time dependence. *Journal of Fluid Mechanics*, 67(4), 705–722. https://doi.org/10.1017/s0022112075000560

Bell, T. H. (1975b). Topographically generated internal waves in the open ocean. *Journal of Geophysical Research*, 80(3), 320–327. https://doi.org/10.1029/JC080i003p00320

Brearley, J. A., Sheen, K. L., Naveira Garabato, A. C., Smeed, D. A., & Waterman, S. (2013). Eddy-induced modulation of turbulent dissipation over rough topography in the Southern Ocean. *Journal of Physical Oceanography*, 43(11), 2288–2308. https://doi.org/10.1175/jpo-d-12-0222.1

Bühler, O., & McIntyre, M. E. (2005). Wave capture and wave-vortex duality. *Journal of Fluid Mechanics*, 534(July 2005), 67–95. https://doi.org/10.1017/S0022112005004374

Cusack, J. M., Alexander Brearley, J., Naveira Garabato, A. C., Smeed, D. A., Polzin, K. L., Velzeboer, N., & Shakespeare, C. J. (2020). Observed eddy–internal wave interactions in the Southern Ocean. *Journal of Physical Oceanography*, 50(10), 3043–3062. https://doi.org/10.1175/JPO-D-20-0001.1

Dee, D. P., Uppala, S. M., Simmons, A. J., Berrisford, P., Poli, P., Kobayashi, S., et al. (2011). The ERA-Interim reanalysis: Configuration and performance of the data assimilation system. *Quarterly Journal of the Royal Meteorological Society*, 137(656), 553–597. https://doi.org/10.1002/qj.828

Eden, C., Olbers, D., & Eriksen, T. (2021). A Closure for Lee Wave Drag on the Large-Scale Ocean Circulation. *Journal of Physical Oceanography*, 51(12), 3573–3588. https://doi.org/10.1175/JPO-D-20-0230.1

Eliassen, A., & Palm, T. (1960). On the transfer of energy in stationary mountain waves. Geofysiske Publikasjoner, 22(3), 1–23

Goff, J. A., & Jordan, T. H. (1988). Stochastic modeling of seafloor morphology: Inversion of sea beam data for second-order statistics. *Journal of Geophysical Research: Solid Earth*, 93(B11), 13589–13608. https://doi.org/10.1029/JB093iB11p13589

Jing, Z., Chang, P., Dimarco, S. F., & Wu, L. (2018). Observed energy exchange between low-frequency flows and internal waves in the Gulf of Mexico. *Journal of Physical Oceanography*, 48(4), 995–1008. https://doi.org/10.1175/JPO-D-17-0263.1

Klymak, J. M. (2018). Nonpropagating form drag and turbulence due to stratified flow over large-scale abyssal-hill topography. *Journal of Physical Oceanography*, 48, 2383–2395. https://doi.org/10.1175/jpo-d-17-0225.1

Kunze, E., & Lien, R. C. (2019). Energy sinks for lee waves in shear flow. *Journal of Physical Oceanography*, 49, 2851–2865. https://doi.org/10.1175/jpo-d-19-0052.1

Large, W. G., McWilliams, J. C., & Doney, S. C. (1994). Oceanic vertical mixing: A review and a model with a nonlocal boundary layer parameterization. *Reviews of Geophysics*, 32(4), 363–403. https://doi.org/10.1029/94RG01872

Leaman, K. D., & Sanford, T. B. (1975). Vertical energy propagation of inertial waves: A vector spectral analysis of velocity profiles. *Journal of Geophysical Research*, 80(15), 1975-1978. https://doi.org/10.1029/jc080i015p01975

Marshall, D. P., & Naveira Garabato, A. C. (2008). A conjecture on the role of bottom-enhanced diapycnal mixing in the parameterization of geostrophic eddies. *Journal of Physical Oceanography*, 38(7), 1607–1613. https://doi.org/10.1175/2007JPO3619.1

Marshall, J., Adcroft, A., Hill, C., Perelman, L., & Heisey, C. (1997). A finite-volume, incompressible Navier-Stokes model for studies of the ocean on parallel computers. *Journal of Geophysical Research*, 102, 5753–5766. https://doi.org/10.1029/96JC02775

Molemaker, M. J., McWilliams, J. C., & Yavneh, I. (2005). Baroclinic instability and loss of balance. *Journal of Physical Oceanography*, 35(9), 1505–1517. https://doi.org/10.1175/JPO2770.1

Müller, P. (1976). On the diffusion of momentum and mass by internal gravity waves. *Journal of Fluid Mechanics*, 77(4), 789–823. https://doi.org/10.1017/s0022112076002899

Nagai, T., Tandon, A., Kunze, E., & Mahadevan, A. (2015). Spontaneous generation of near-inertial waves by the Kuroshio Front. *Journal of Physical Oceanography*, 45(9), 2381–2406. https://doi.org/10.1175/JPO-D-14-0086.1

Naveira Garabato, A., Polzin, K. L., King, B. A., Heywood, K. J., & Visbeck, M. (2004). Widespread intense turbulent mixing in the Southern Ocean. *Science*, 303, 210–213. https://doi.org/10.1126/science.1090929

Nikurashin, M., & Ferrari, R. (2010a). Radiation and dissipation of internal waves generated by geostrophic flows impinging on small-scale topography: Theory. *Journal of Physical Oceanography*, 40, 1055–1074. https://doi.org/10.1175/2009jpo4199.1

Nikurashin, M., & Ferrari, R. (2010b). Radiation and dissipation of internal waves generated by geostrophic flows impinging on small-scale topography: Application to the Southern Ocean. *Journal of Physical Oceanography*, 40, 2025–2042. https://doi.org/10.1175/2010jpo4315.1

Nikurashin, M., & Ferrari, R. (2011). Global energy conversion rate from geostrophic flows into internal lee waves in the deep ocean. *Geophysical Research Letters*, 38, L08610. https://doi.org/10.1029/2011gl046576

Nikurashin, M., Ferrari, R., Grisouard, N., & Polzin, K. (2014). The impact of finite-amplitude bottom topography on internal wave generation in the Southern Ocean. *Journal of Physical Oceanography*, 44, 2938–2950. https://doi.org/10.1175/jpo-d-13-0201.1

Nikurashin, M., Vallis, G. K., & Adcroft, A. (2013). Routes to energy dissipation for geostrophic flows in the Southern Ocean. *Nature Geoscience*, 6(1), 48–51. https://doi.org/10.1038/ngeo1657

Provenzale, A. (1999). Transport by coherent barotropic vortices. *Annual Review of Fluid Mechanics*, 31, 55–93. https://doi.org/10.1146/annurev.fluid.31.1.55

Scott, R. B., Goff, J. A., Naveira Garabato, A. C., & Nurser, A. J. G. (2011). Global rate and spectral characteristics of internal gravity wave generation by geostrophic flow over topography. *Journal of Geophysical Research*, 116, C09029. https://doi.org/10.1029/2011jc007005

Shakespeare, C. (2020). Interdependence of internal tide and lee wave generation at abyssal hills: Global calculations. *Journal of Physical Oceanography*, 50, 655–677. https://doi.org/10.1175/jpo-d-19-0179.1

Shakespeare, C. J., & Hogg, A. M. C. (2017). Spontaneous surface generation and interior amplification of internal waves in a regional-scale ocean model. *Journal of Physical Oceanography*, 47(4), 811–826. https://doi.org/10.1175/JPO-D-16-0188.1

Sheen, K. L., Brearley, J. A., Naveira Garabato, A. C., Smeed, D. A., Waterman, S., Ledwell, J. R., et al. (2013). Rates and mechanisms of turbulent dissipation and mixing in the Southern Ocean: Results from the Diapycnal and Isopycnal Mixing Experiment in the Southern Ocean (DIMES). *Journal of Geophysical Research*, 118, 2774–2792. https://doi.org/10.1002/jgrc.20217

Sun, H., Yang, Q., Zheng, K., Zhao, W., Huang, X., & Tian, J. (2022). Internal lee waves generated by shear flow over small-scale topography. *Journal of Geophysical Research: Oceans*, 127, e2022JC018547. https://doi.org/10.1029/2022JC018547

Trosman, D. S., Waterman, S., Polzin, K. L., Arbic, B. K., Garner, S. T., Naveira Garabato, A. C., & Sheen, K. L. (2015). Internal lee wave closures: Parameter sensitivity and comparison to observations. *Journal of Geophysical Research*, 120, 7997–8019. https://doi.org/10.1002/2015jc010892

Waterman, S., Naveira Garabato, A., & Polzin, K. (2013). Internal waves and turbulence in the Antarctic Circumpolar Current. *Journal of Physical Oceanography*, 43, 259–282. https://doi.org/10.1175/JPO-D-11-0194.1

Waterman, S., Polzin, K., Naveira Garabato, A., Shen, K., & Forryan, A. (2014). Suppression of internal wave breaking in the Antarctic Circumpolar Current near topography. *Journal of Physical Oceanography*, 44, 1466–1492. https://doi.org/10.1175/jpo-d-12-0154.1

Wright, C. J., Scott, R. B., Ailliot, P., & Furnival, D. (2014). Lee wave generation rates in the deep ocean. *Geophysical Research Letters*, 41, 2434–2440. https://doi.org/10.1002/2013gl059087

Wurtele, M. G., Sharman, R. D., & Datta, A. (1996). Atmospheric lee waves. *Annual Review of Fluid Mechanics*, 28, 429–476. https://doi.org/10.1146/annurev.fl.28.010196.002241

Yang, Z., Jing, Z. & Zhai, X. (2022). Effect of Small-scale Topography on Eddy Dissipation in the Northern South China Sea. *Journal of Physical Oceanography*. https://doi.org/10.1175/JPO-D-21-0208.1

Yang, Z., Zhai, X., Marshall, D. P., & Wang, G. (2021). An Idealized Model Study of Eddy Energetics in the Western Boundary "Graveyard." *Journal of Physical Oceanography*, 51(4), 1265–1282. https://doi.org/10.1175/jpo-d-19-0301.1

Zemskova, V. E., & Grisouard, N. (2021). Near-inertial dissipation due to stratified flow over abyssal topography. *Journal of Physical Oceanography*, (2), 2483–2504. https://doi.org/10.1175/jpo-d-21-0007.1

Zemskova, V. E., & Grisouard, N. (2022). Energetics and Mixing of Stratified, Rotating Flow over Abyssal Hills. *Journal of Physical Oceanography*, 52(6), 1155–1177. https://doi.org/10.1175/jpo-d-21-0146.1

Zheng, K., & Nikurashin, M. (2019). Downstream propagation and remote dissipation of internal waves in the southern ocean. *Journal of Physical Oceanography*, 49(7), 1873–1887. https://doi.org/10.1175/JPO-D-18-0134.1